LETTER

doi:10.1038/nature17402

Structural basis of cohesin cleavage by separase

Zhonghui Lin[1,2], Xuelian Luo[2,3] & Hongtao Yu[1,2]

Accurate chromosome segregation requires timely dissolution of chromosome cohesion after chromosomes are properly attached to the mitotic spindle. Separase is absolutely essential for cohesion dissolution in organisms from yeast to man[1,2]. It cleaves the kleisin subunit of cohesin and opens the cohesin ring to allow chromosome segregation. Cohesin cleavage is spatiotemporally controlled by separase-associated regulatory proteins, including the inhibitory chaperone securin[3–6], and by phosphorylation of both the enzyme and substrates[7–12]. Dysregulation of this process causes chromosome missegregation and aneuploidy, contributing to cancer and birth defects. Despite its essential functions, atomic structures of separase have not been determined. Here we report crystal structures of the separase protease domain from the thermophilic fungus *Chaetomium thermophilum*, alone or covalently bound to unphosphorylated and phosphorylated inhibitory peptides derived from a cohesin cleavage site. These structures reveal how separase recognizes cohesin and how cohesin phosphorylation by polo-like kinase 1 (Plk1) enhances cleavage. Consistent with a previous cellular study[13], mutating two securin residues in a conserved motif that partly matches the separase cleavage consensus converts securin from a separase inhibitor to a substrate. Our study establishes atomic mechanisms of substrate cleavage by separase and suggests competitive inhibition by securin.

Separase belongs to the clan CD family of cysteine proteases which includes caspases[1]. It contains a large amino (N)-terminal armadillo (ARM) repeat domain and a highly conserved carboxy (C)-terminal separase protease domain (SPD) that consists of a pseudo-protease domain (PPD) and an active protease domain (APD)[14] (Fig. 1a and Extended Data Fig. 1). Cohesin forms an asymmetric ring to topologically entrap chromosomes (Fig. 1a)[15,16]. Separase cleaves the kleisin subunit to open the cohesin ring and trigger chromosome segregation. It also cleaves other substrates to regulate anaphase spindle elongation and centriole duplication[17,18]. High-resolution structures of separase have not been determined more than a decade

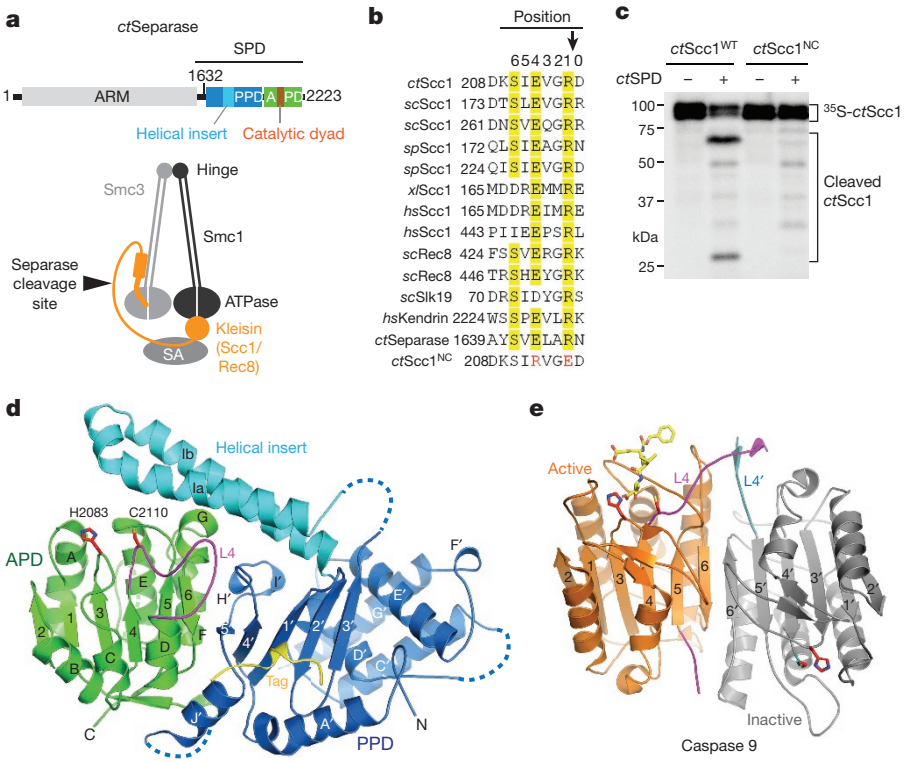

Figure 1 | Structure of *ct*SPD. a, Domains and motifs of separase from *C. thermophilum* (top) and schematic drawing of cohesin (bottom). **b**, Sequence alignment of the cleavage sites of separase substrates; *sc*, *Saccharomyces cerevisiae*; *sp*, *Schizosaccharomyces pombe*; *xl*, *Xenopus laevis*; *hs*, *Homo sapiens*. **c**, Autoradiograph of the *ct*SPD cleavage assay with ^{35}S-*ct*Scc1 wild type (WT) or non-cleavable mutant (NC) as substrates. For gel source data, see Supplementary Fig. 1. **d**, Cartoon of the crystal structure of *ct*SPD. L4 is coloured magenta. Loops with no visible electron densities are indicated by dashed lines. **e**, Cartoon of caspase 9 (Protein Data Bank accession number 1JXQ), with the bound inhibitor shown as yellow sticks.

[1]Howard Hughes Medical Institute, University of Texas Southwestern Medical Center, 6001 Forest Park Road, Dallas, Texas 75390, USA. [2]Department of Pharmacology, University of Texas Southwestern Medical Center, 6001 Forest Park Road, Dallas, Texas 75390, USA. [3]Department of Biophysics, University of Texas Southwestern Medical Center, 6001 Forest Park Road, Dallas, Texas 75390, USA.

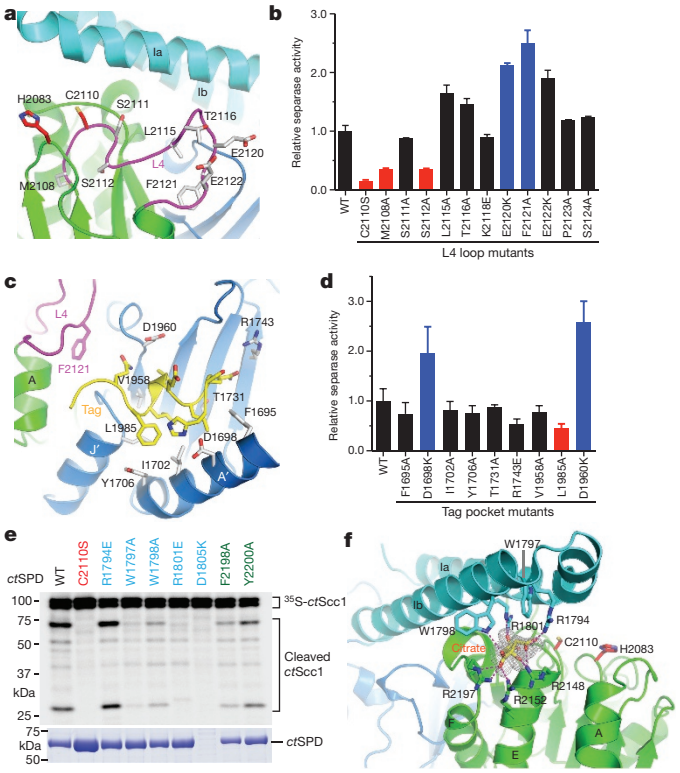

Figure 2 | Contributions of the L4 loop and the helical insert to the activity of *ct*SPD. a, Cartoon of *ct*SPD with the catalytic dyad and L4 loop residues shown. **b**, **d**, Quantification of the protease activity of *ct*SPD WT and mutants (mean ± s.d., $n = 3$ independent experiments). Mutants with activities greater or less than twofold that of WT are in blue and red, respectively. **c**, Interactions between the N-terminal tag and a surface pocket of *ct*SPD. **e**, Autoradiograph of the ^{35}S-*ct*Scc1 cleavage assay by *ct*SPD WT or mutants. Bottom: Coomassie-stained gel of *ct*SPD proteins. **f**, A conserved basic pocket in *ct*SPD, with the $2F_o - F_c$ map of the bound citrate shown at 2.0σ.

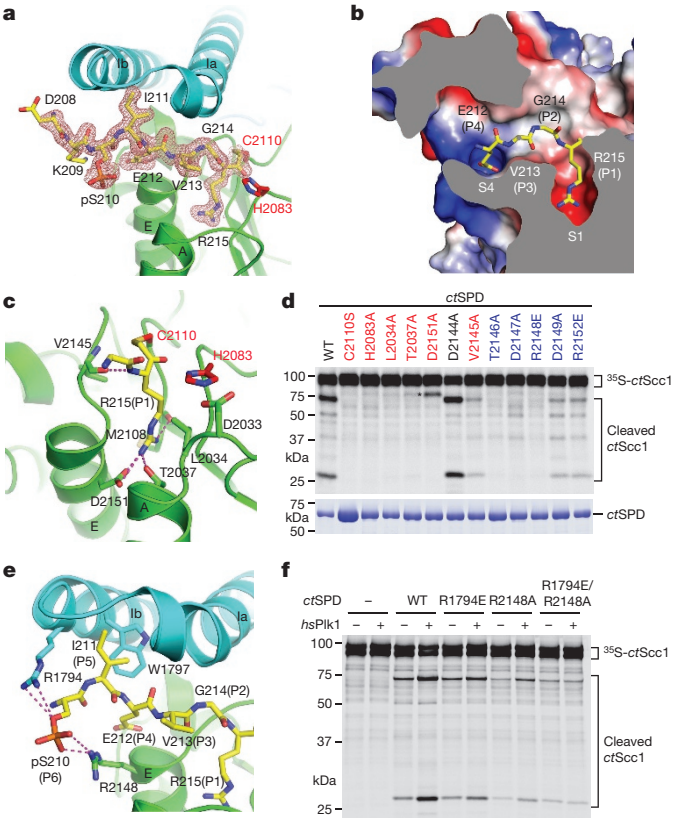

Figure 3 | Structural basis of Scc1 cleavage by separase. a, Cartoon of *ct*SPD bound to pAMK (shown as sticks overlaid with the $2F_o - F_c$ map at 1.0σ). **b**, Cross-sectional view of the surface drawing of *ct*SPD–*ct*Scc1 coloured with its electrostatic potential (blue, positive; red, negative; white, neutral). The bound Scc1 peptide is shown as sticks. **c**, The S1 pocket of *ct*SPD that recognizes the P1 arginine. Dashed lines indicate hydrogen bonds or favourable electrostatic interactions. **d**, Autoradiograph of the cleavage reaction of *ct*SPD WT and mutants with ^{35}S-*ct*Scc1 as substrate. Active-site/S1 mutants are labelled red; S4 mutants are labelled blue. Bottom: Coomassie-stained gel of the *ct*SPD proteins. Asterisk marks an aberrant cleavage product of D2151A. **e**, The pS210-binding site. **f**, Autoradiograph of the cleavage reactions of *ct*SPD WT and mutants with ^{35}S-*ct*Scc1 as substrate, with or without a prior incubation with *hs*Plk1.

since its discovery, hindering our understanding of its mechanism and regulation.

We found that SPD of *C. thermophilum* (*ct*) separase could be expressed in large quantities in bacteria without securin (Extended Data Fig. 2a). Recombinant *ct*SPD, but not the C2110S mutant, cleaved *ct*Scc1 to produce two major fragments (Extended Data Fig. 2b). Separase is known to cleave after the EXXR (X, any residue) consensus motif[2]. Charge-reversal mutation of the ^{212}EVGR^{215} motif in *ct*Scc1 reduced cleavage by separase (Fig. 1b, c). An acyloxymethyl ketone (AMK)-containing peptide inhibitor derived from this cleavage site blocked *ct*Scc1 cleavage in a dose-dependent manner (Extended Data Fig. 2c, d), and retarded the gel mobility of *ct*SPD^{WT}, but not *ct*SPD^{C2110S}, consistent with covalent inhibition (Extended Data Fig. 2e). Similar to separases from other species[6], longer constructs of *ct*SPD containing an N-terminal extension underwent autocleavage at the ^{1643}ELAR^{1646} site (Fig. 1b and Extended Data Fig. 2f). Thus, recombinant *ct*SPD was active.

We determined the crystal structure of *ct*SPD (Fig. 1d and Extended Data Table 1). It forms one globular domain with two sub-domains—the PPD and the APD—that pack against each other. APD has an overall fold similar to that of caspases (Fig. 1d, e and Extended Data Figs 3 and 4a). PPD also has a mixed α/β fold, but its central β-sheet has a topology different from that of caspases. One edge of this central sheet of PPD forms an edge-on interaction with that of APD, whereas the other edge is capped by a helical domain in PPD. A prominent helical insert of PPD forms a long coiled-coil and packs against APD.

The catalytic dyad H2083 and C2110 are located in loops L3 and L4 of APD (Fig. 1d and Extended Data Fig. 3a). An important mechanism of pro-caspase activation is the reorganization of L4, which can be achieved through homo-dimerization, cleavage of an internal linker, or both[19–22]. The geometry of the catalytic dyad and the extended conformation of L4 in *ct*SPD are similar to those in active caspase 9 (Fig. 1d, e), consistent with *ct*SPD being an active enzyme. Thus, separase activation does not require proteolytic cleavage of L4. Consistent with the importance of the L4 loop, mutations of two residues adjacent to C2110, M2108 and S2112, reduced the activity of *ct*SPD (Fig. 2a, b and Extended Data Fig. 4b). In contrast, mutations of L4 residues distal to C2110, including E2120 and F2121, enhanced the activity of *ct*SPD.

A segment of the N-terminal tag of recombinant *ct*SPD binds to a conserved surface pocket in PPD adjacent to L4 (Figs 1d, 2c and Extended Data Fig. 4c). Although this tag is not required for the activity of *ct*SPD, mutations targeting residues in the tag-binding pocket altered the activity of *ct*SPD containing the tag (Fig. 2d and Extended Data Fig. 4d). Similar to mutations of the distal L4 residues, the D1698K and D1960K mutations enhanced the activity of *ct*SPD. We propose that securin or other regions of separase may bind to this tag-binding site, alter the conformation of L4, and affect the protease activity of separase. Even without bona fide ligands, binding of an artificial tag to this site can regulate the protease activity of *ct*SPD in a subtle way.

Unlike active caspase 9, which forms a homodimer[19], separase contains an internal PPD in the same polypeptide chain that packs

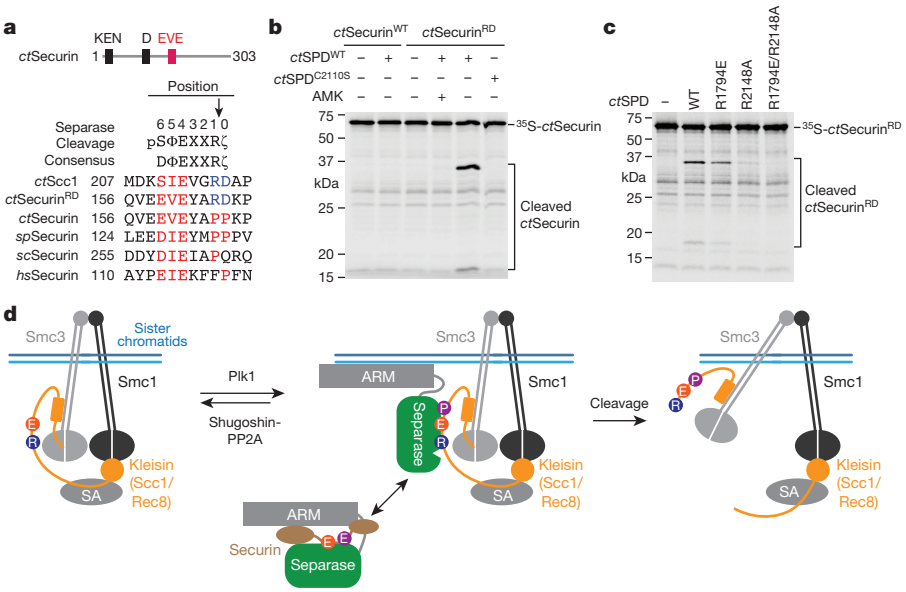

Figure 4 | Securin as a pseudo-substrate of separase. a, Sequence alignment of the EVE motif of securin, with the separase cleavage consensus shown above. The KEN and destruction boxes (D) are indicated. Φ/ζ, hydrophobic/hydrophilic residues. **b**, Autoradiograph of the cleavage reactions of ^{35}S-*ct*securin WT or P164R/P165D (RD) by *ct*SPD WT or C2110S with or without the AMK inhibitor. **c**, Autoradiograph of the cleavage reactions of ^{35}S-*ct*securinRD by the indicated *ct*SPD proteins. **d**, Model depicting specificity determinants, phospho-regulation, and securin inhibition of separase-dependent cohesin cleavage. SA, stromal antigen. Cohesin cleavage by separase can be stimulated by DNA[30]. The ARM domain of separase might contact DNA.

against and stabilizes its APD. In particular, the helical insert of PPD makes extensive contacts with APD and bridges the two sub-domains (Extended Data Fig. 5a, b). Deletion of the helical insert or mutations of key residues at the helical insert–APD interface, including D1805 and W2143, abolished the expression of soluble *ct*SPD in bacteria (Fig. 2e and Extended Data Fig. 5a–c). Several helical-insert residues, including C1782 and H1783, are located close to the active site (Extended Data Fig. 5a). Mutations of these residues did not affect the solubility of *ct*SPD, but reduced the protease activity (Extended Data Fig. 5d). Moreover, residues from the tip of the helical insert, along with residues from APD, form a basic pocket that binds a citrate molecule (Fig. 2f). Mutations of these conserved residues, with the exception of R1794E, diminished separase activity (Fig. 2e and Extended Data Fig. 1). Therefore, the helical insert is critical for both the structure integrity and activity of separase.

Phosphorylation of Scc1 by Plk1 enhances Scc1 cleavage by separase[10,11]. This cleavage-enhancing phosphorylation is opposed by the shugoshin–PP2A complex bound to cohesin[23–27]. Incubation of *ct*Scc1, but not *ct*Scc1 S210A, with human Plk1 (*hs*Plk1) enhanced the cleavage of *ct*Scc1 by *ct*SPD (Extended Data Fig. 6a). Addition of the *hs*Plk1 inhibitor BI2536 blocked this enhancement. The phospho-mimicking S210E mutation stimulated *ct*Scc1 cleavage by separase (Extended Data Fig. 6b). Thus, Plk1-dependent phosphorylation of *ct*Scc1 at S210 enhances Scc1 cleavage by separase.

We next determined the crystal structures of *ct*SPD bound to unphosphorylated (AMK) or phospho-S210-containing (pAMK) inhibitors (Extended Data Table 1). The overall structure of *ct*SPD–AMK and *ct*SPD–pAMK complexes is virtually identical to that of free *ct*SPD, indicating that substrate binding does not induce notable conformational changes. Only the C-terminal ^{212}EVGR^{215} segment of the unphosphorylated AMK inhibitor was visible (Extended Data Fig. 6c), whereas all residues of the pAMK inhibitor had clearly defined electron density (Fig. 3a). In both structures, the active-site cysteine C2110 is covalently linked to *ct*Scc1 R215 at the P1 position. Consistent with its role in stabilizing the oxyanion during catalysis, *ct*SPD H2083 of the catalytic dyad is located close to carbonyl group of *ct*Scc1 R215. R215 forms a salt bridge with *ct*SPD D2151 at the base of a deep, acidic S1 pocket (Fig. 3b, c). *ct*Scc1 E212 at P4 inserts into the aforementioned citrate-binding pocket, forming favourable electrostatic and hydrogen bonding interactions (Fig. 3b and Extended Data Fig. 6d). *ct*Scc1 V213 and G214 form minimal contacts with *ct*SPD. Mutations of residues lining the S1 and S4 pockets in *ct*SPD greatly diminished separase activity (Fig. 3d).

The S1 pocket mutant D2151A of *ct*SPD cleaved *ct*Scc1 at a different site (Fig. 3d). The *ct*Scc1 E180K mutation abolished this aberrant cleavage (Extended Data Fig. 6e), indicating that the mutant separase cleaved the ^{180}ELGM^{183} site. Thus, D2151 not only selects for basic residues but also discriminates against hydrophobic residues at P1. *ct*SPD charge reversal mutants D2151R and R2152E did not efficiently cleave the complementary charge reversal mutants of *ct*Scc1 (Extended Data Fig. 6f), indicating that other residues in the S1 and S4 pockets contribute to substrate recognition. Because most residues lining the S1 and S4 pockets are conserved among separases in all species (Extended Data Figs 1 and 7), our analyses establish the basis for the EXXR substrate specificity of separase.

Phosphorylation of the substrate does not alter the binding mode of EVGR at P1–P4, but reveals or establishes additional contacts at P5 and P6. I211 at the P5 position packs against W1797 of the helical insert (Fig. 3e). *ct*Scc1 I211A was less efficiently cleaved by *ct*SPD with or without Plk1 (Extended Data Fig. 8a). Thus, as reported previously[28], the hydrophobic residue at P5 contributes to substrate specificity. Phospho-S210 at P6 makes favourable electrostatic interactions with R1794 of the helical insert and R2148 of APD in *ct*SPD (Fig. 3e and Extended Data Fig. 8b). Single mutation of R1794 or R2148 reduced the stimulation of Scc1 cleavage by Plk1, whereas the double mutation abolished the effect (Fig. 3f and Extended Data Fig. 8c, d). Unlike R2148A, R1794E does not affect the cleavage of unphosphorylated Scc1. Therefore, R1794 specifically serves as a receptor for pS210. R2148 contributes to the recognition of both pS210 and E212. The serine at P6 is conserved in fungal Scc1 and other separase substrates (Fig. 1b). The N-terminal separase cleavage site in vertebrate Scc1 contains a phospho-mimicking, acidic residue at that position. Our structures thus explain the phosphorylation dependency of cohesin cleavage, and further suggest that this phospho-regulation might apply to other separase substrates.

Finally, we probed the mechanism by which securin inhibits separase. Securin blocks substrate access to the active site of separase[3,6].

Expectedly, the *ct*securin–*ct*separase complex was less active in *ct*Scc1 cleavage, compared with *ct*SPD (Extended Data Fig. 9a, b). A conserved EVE motif in securin matches the separase cleavage consensus at positions P2–P6, but lacks the arginine at P1 and often has a proline at P0 instead of a hydrophilic residue (Fig. 4a). A securin mutant with three residues in this motif mutated was cleaved by separase in fission yeast cells[13]. We thus mutated P164 and P165 in *ct*securin to R and D, the matching *ct*Scc1 residues at P1 and P0. The resulting *ct*securinRD mutant was efficiently cleaved by *ct*SPD, and this cleavage was inhibited by the AMK inhibitor (Fig. 4b). Mutating the phosphoserine-binding residues in *ct*SPD or E159 in *ct*securinRD reduced cleavage (Fig. 4c and Extended Data Fig. 9c), indicating that this artificial substrate bound at the canonical substrate-binding sites of separase. *ct*securin bound tightly to the N-terminal ARM domain of *ct*separase (Extended Data Fig. 9d). A synthetic EVE-containing securin peptide did not inhibit *ct*SPD (Extended Data Fig. 9e). We propose that securin acts as a pseudo-substrate to competitively block substrate binding to separase (Fig. 4d). Securin binding to the ARM domain of separase provides the necessary avidity for securin to outcompete authentic substrates for access to the active site. Securin is not cleaved because of incompatible residues at the site of cleavage.

As a crucial protease that triggers chromosome segregation, separase is a potential oncoprotein[29]. Because of the conserved principles of substrate recognition (Extended Data Fig. 7), our structure of an active fungal separase can guide the rational design of chemical inhibitors of human separase, which may have therapeutic potential.

Online Content Methods, along with any additional Extended Data display items and Source Data, are available in the online version of the paper; references unique to these sections appear only in the online paper.

Received 2 November 2015; accepted 5 February 2016.
Published online 30 March 2016.

1. Uhlmann, F., Wernic, D., Poupart, M. A., Koonin, E. V. & Nasmyth, K. Cleavage of cohesin by the CD clan protease separin triggers anaphase in yeast. *Cell* **103,** 375–386 (2000).
2. Hauf, S., Waizenegger, I. C. & Peters, J. M. Cohesin cleavage by separase required for anaphase and cytokinesis in human cells. *Science* **293,** 1320–1323 (2001).
3. Hornig, N. C., Knowles, P. P., McDonald, N. Q. & Uhlmann, F. The dual mechanism of separase regulation by securin. *Curr. Biol.* **12,** 973–982 (2002).
4. Ciosk, R. *et al.* An ESP1/PDS1 complex regulates loss of sister chromatid cohesion at the metaphase to anaphase transition in yeast. *Cell* **93,** 1067–1076 (1998).
5. Zou, H., McGarry, T. J., Bernal, T. & Kirschner, M. W. Identification of a vertebrate sister-chromatid separation inhibitor involved in transformation and tumorigenesis. *Science* **285,** 418–422 (1999).
6. Waizenegger, I., Giménez-Abián, J. F., Wernic, D. & Peters, J. M. Regulation of human separase by securin binding and autocleavage. *Curr. Biol.* **12,** 1368–1378 (2002).
7. Stemmann, O., Zou, H., Gerber, S. A., Gygi, S. P. & Kirschner, M. W. Dual inhibition of sister chromatid separation at metaphase. *Cell* **107,** 715–726 (2001).
8. Gorr, I. H., Boos, D. & Stemmann, O. Mutual inhibition of separase and Cdk1 by two-step complex formation. *Mol. Cell* **19,** 135–141 (2005).
9. Hellmuth, S. *et al.* Human chromosome segregation involves multi-layered regulation of separase by the peptidyl-prolyl-isomerase Pin1. *Mol. Cell* **58,** 495–506 (2015).
10. Alexandru, G., Uhlmann, F., Mechtler, K., Poupart, M. A. & Nasmyth, K. Phosphorylation of the cohesin subunit Scc1 by Polo/Cdc5 kinase regulates sister chromatid separation in yeast. *Cell* **105,** 459–472 (2001).
11. Hauf, S. *et al.* Dissociation of cohesin from chromosome arms and loss of arm cohesion during early mitosis depends on phosphorylation of SA2. *PLoS Biol.* **3,** e69 (2005).
12. Katis, V. L. *et al.* Rec8 phosphorylation by casein kinase 1 and Cdc7-Dbf4 kinase regulates cohesin cleavage by separase during meiosis. *Dev. Cell* **18,** 397–409 (2010).
13. Nagao, K. & Yanagida, M. Securin can have a separase cleavage site by substitution mutations in the domain required for stabilization and inhibition of separase. *Genes Cells* **11,** 247–260 (2006).
14. Viadiu, H., Stemmann, O., Kirschner, M. W. & Walz, T. Domain structure of separase and its binding to securin as determined by EM. *Nature Struct. Mol. Biol.* **12,** 552–553 (2005).
15. Gligoris, T. G. *et al.* Closing the cohesin ring: structure and function of its Smc3-kleisin interface. *Science* **346,** 963–967 (2014).
16. Huis in 't Veld, P. J. *et al.* Characterization of a DNA exit gate in the human cohesin ring. *Science* **346,** 968–972 (2014).
17. Sullivan, M., Lehane, C. & Uhlmann, F. Orchestrating anaphase and mitotic exit: separase cleavage and localization of Slk19. *Nature Cell Biol.* **3,** 771–777 (2001).
18. Matsuo, K. *et al.* Kendrin is a novel substrate for separase involved in the licensing of centriole duplication. *Curr. Biol.* **22,** 915–921 (2012).
19. Renatus, M., Stennicke, H. R., Scott, F. L., Liddington, R. C. & Salvesen, G. S. Dimer formation drives the activation of the cell death protease caspase 9. *Proc. Natl Acad. Sci. USA* **98,** 14250–14255 (2001).
20. Chai, J. *et al.* Structural basis of caspase-7 inhibition by XIAP. *Cell* **104,** 769–780 (2001).
21. Srinivasula, S. M., Ahmad, M., Fernandes-Alnemri, T. & Alnemri, E. S. Autoactivation of procaspase-9 by Apaf-1-mediated oligomerization. *Mol. Cell* **1,** 949–957 (1998).
22. Shi, Y. Caspase activation: revisiting the induced proximity model. *Cell* **117,** 855–858 (2004).
23. Kitajima, T. S. *et al.* Shugoshin collaborates with protein phosphatase 2A to protect cohesin. *Nature* **441,** 46–52 (2006).
24. Riedel, C. G. *et al.* Protein phosphatase 2A protects centromeric sister chromatid cohesion during meiosis I. *Nature* **441,** 53–61 (2006).
25. Tang, Z. *et al.* PP2A is required for centromeric localization of Sgo1 and proper chromosome segregation. *Dev. Cell* **10,** 575–585 (2006).
26. Ishiguro, T., Tanaka, K., Sakuno, T. & Watanabe, Y. Shugoshin-PP2A counteracts casein-kinase-1-dependent cleavage of Rec8 by separase. *Nature Cell Biol.* **12,** 500–506 (2010).
27. Liu, H., Rankin, S. & Yu, H. Phosphorylation-enabled binding of SGO1–PP2A to cohesin protects sororin and centromeric cohesion during mitosis. *Nature Cell Biol.* **15,** 40–49 (2013).
28. Sullivan, M., Hornig, N. C., Porstmann, T. & Uhlmann, F. Studies on substrate recognition by the budding yeast separase. *J. Biol. Chem.* **279,** 1191–1196 (2004).
29. Zhang, N. *et al.* Overexpression of separase induces aneuploidy and mammary tumorigenesis. *Proc. Natl Acad. Sci. USA* **105,** 13033–13038 (2008).
30. Sun, Y. *et al.* Separase is recruited to mitotic chromosomes to dissolve sister chromatid cohesion in a DNA-dependent manner. *Cell* **137,** 123–132 (2009).

Supplementary Information is available in the online version of the paper.

Acknowledgements We thank D. Rosenbaum for the *C. thermophilum* complementary DNA, H. Ball for peptide synthesis, and D. Tomchick and Z. Chen for assistance with data collection. Diffraction data of the selenomethionine separase were collected at the Advanced Light Source at Lawrence Berkeley National Laboratory with the help of its staff. The Advanced Light Source is supported by the Director, Office of Science, Office of Basic Energy Sciences, of the US Department of Energy under contract number DE-AC02-05CH11231. Results shown in this report are derived from work performed at Argonne National Laboratory, Structural Biology Center at the Advanced Photon Source. Argonne is operated by UChicago Argonne, LLC, for the US Department of Energy, Office of Biological and Environmental Research under contract DE-AC02-06CH11357. This work is supported by the Cancer Prevention and Research Institute of Texas (RP110465-P3 to H.Y.), the National Institutes of Health (GM107415 to X.L.), and the Welch Foundation (I-1441 to H.Y.). H.Y. is an investigator with the Howard Hughes Medical Institute.

Author Contributions Z.L. performed all experiments in this study with advice from H.Y. X.L. provided assistance with structure refinement. Z.L. and H.Y. wrote the paper.

Author Information Atomic coordinates and structure factors have been deposited in the Protein Data Bank under accession numbers 5FBY, 5FC3, and 5FC2. Reprints and permissions information is available at www.nature.com/reprints. The authors declare no competing financial interests. Readers are welcome to comment on the online version of the paper. Correspondence and requests for materials should be addressed to H.Y. (hongtao.yu@utsouthwestern.edu).

METHODS

No statistical methods were used to predetermine sample size. The experiments were not randomized. The investigators were not blinded to allocation during experiments and outcome assessment.

Expression and purification of *ct*SPD. The *ct*separase cDNA (GenBank identity 18261092) was synthesized at GenScript USA. For the expression of the *ct*SPD, the cDNA fragment of *ct*SPD$^{1632–2223}$ was subcloned into a modified pET bacterial expression vector. The pET-*ct*SPD vector encoded *ct*SPD$^{1632–2223}$ with an N-terminal His_6 tag of the following sequence: MGSSHHHHHHSQLEVLFQGPLGSGRP. The pET-*ct*SPD vector was transformed into *Escherichia coli* strain BL21(DE3). Protein expression was induced with isopropylthiogalactoside (IPTG) at 18 °C overnight. The bacteria were harvested and resuspended in the lysis buffer (50 mM Tris-HCl, pH 8.0, 200 mM NaCl, 5% glycerol, 1 mM DTT, and 0.05% Triton X-100). After sonication and centrifugation, the supernatant was applied to Ni^{2+}-NTA resin (Qiagen). After extensive washing, His_6-*ct*SPD was eluted from the Ni^{2+}-NTA column. His_6-*ct*SPD was further purified with a mono Q 5/50 GL anion-exchange column (GE Healthcare) and a Superdex 200 10/300 GL column. The point mutants of *ct*SPD were generated with a QuikChange Lightning Site-Directed Mutagenesis kit (Agilent Technologies). The truncated variants and point mutants of *ct*SPD were expressed and purified similarly. Because *ct*SPD$^{1632–2223}$ underwent autocleavage at the ^{1643}ELAR^{1646} site, we generated a non-cleavable ^{1643}RLAE^{1646} mutant to prevent autocleavage and increase yield. All *ct*SPDs in this study, except that in Extended Data Fig. 2f, contained the non-cleavable mutation.

The selenomethionine (SeMet)-labelled *ct*SPD$^{1663–2223}$ was produced with the methionine biosynthesis inhibition method[31]. Briefly, bacteria transformed with pET-*ct*SPD cultured overnight were pelleted, washed, and resuspended with M9 minimal media. The bacteria were further incubated at 37 °C until the absorbance at 600 nm reached about 1.0. Methionine biosynthesis was inhibited by the addition of the amino-acid solution containing 50 mg l^{-1} of Leu/Ile/Val and 100 mg l^{-1} of Phe/Lys/Thr/SeMet. Protein expression was induced with 0.4 mM ITPG at 18 °C overnight. The SeMet-labelled protein was subsequently purified through the same procedure as described above.

Expression and purification of *ct*separase–securin complex and *ct*SPD$^{1501-2223}$. The *ct*securin cDNA (GenBank identity 18256826) was cloned from a cDNA library of *C. thermophilum*. The cDNAs of *ct*separase and *ct*securin were separately subcloned into a modified pFastBac HT vector (Invitrogen). The final constructs encoded an N-terminal His_6-Strep-tagged *ct*separase and an N-terminal His_6-tagged *ct*securin. Baculoviruses of *ct*separase (full-length or residues 1-1500) and *ct*securin were constructed with the Bac-to-Bac system (Invitrogen) according to the manufacturer's protocols. Sf9 cells were co-infected with *ct*separase and *ct*securin baculoviruses and harvested at 48 h after infection. Cells were resuspended in the lysis buffer containing 50 mM Tris-HCl, pH 8.0, 200 mM NaCl, 5% glycerol, 1 mM DTT, and 0.05% Triton X-100, followed by sonication and centrifugation. The supernatant was applied onto a Strep-Tactin Superflow column (Qiagen). After extensive washes with the lysis buffer, the *ct*separase–securin complex was eluted with the elution buffer containing 5 mM d-Desthiobiotin (Sigma-Aldrich), 50 mM Tris-HCl, pH 8.0, 200 mM NaCl, 5% glycerol, and 1 mM DTT. The His_6-*ct*SPD$^{1501–2223}$ protein was expressed in Sf9 cells with a similar strategy and purified through a Ni^{2+}-NTA column.

Separase activity assay. The *ct*Scc1 cDNA (GenBank identity 18259702) was synthesized by GenScript USA and was cloned into a modified pCS2 vector with a SP6 promoter. To produce ^{35}S-*ct*Scc1 or its mutants, the pCS2-*ct*Scc1 plasmids were added to a TNT Quick Coupled Transcription Translation System (Promega) and incubated in the presence of ^{35}S-methionine at 30 °C for 90 min. (The ^{35}S-*ct*Scc1 proteins migrated as a doublet on SDS–polyacrylamide gel electrophoresis (SDS–PAGE), possibly owing to proteolysis or internal methionine initiation during the *in vitro* translation reaction.) Then, 2 μl of ^{35}S-*ct*Scc1 was added to 18 μl of *ct*SPD (~1.5 μM) or *ct*separase–securin protein solution containing 25 mM HEPES (pH 7.5), 75 mM KCl, 5 mM $MgCl_2$, 1 mM DTT, 15 mM NaF, 1 mM EGTA, 10% glycerol, and 0.05% Triton X-100, and incubated at 30 °C for 60 min. For assays in Fig. 1c and Extended Data Fig. 2b, a higher concentration of *ct*SPD (3.0 μM) was used, resulting in more complete *ct*Scc1 cleavage. For AMK inhibition assay, *ct*SPD was pre-incubated with the *ct*Scc1-AMK inhibitor (synthesized by KareBay Biochem) at room temperature (25 °C) for 30 min and further incubated with ^{35}S-*ct*Scc1 at 30 °C for 60 min. In the Plk1 stimulation assay, ^{35}S-*ct*Scc1 was pre-treated with recombinant GST-*hs*Plk1^{T210D} in the kinase buffer for 30 min at 30 °C, in the absence or presence of 10 μM BI2536, and further incubated with *ct*SPD (0.5 μM) for 60 min. The reaction mixtures were separated on SDS–PAGE gels, which were stained, destained, dried, and analysed with Fuji or GE phosphoimagers.

The *ct*securin WT and P164R/P165D (*ct*securinRD) cDNAs were subcloned into pCS2-Myc vector with an SP6 promoter. The ^{35}S-*ct*securin^{WT} and *ct*securinRD proteins were produced and assayed as described above. The *ct*securin$_{153–177}$ (DPLQ VE**EVE**YAPPKPKEMPYESDVF) and *ct*securin$_{153–177}$ 3A (DPLQVE**AAA**YAPP KPKEMPYESDVF) peptides were chemically synthesized and tested for their ability to inhibit the cleavage of *ct*Scc1 by *ct*SPD as described above.

Crystallization and data collection. All crystallization experiments were performed at 20 °C. Initial screens were performed with a Phoenix crystallization robot (Art Robbins Instruments), using the commercially available screening kits from Hampton Research, Qiagen, and Molecular Dimensions. Conditions obtained from the initial screens were optimized using hanging-drop vapour diffusion method. Diffraction-quality crystals were obtained by repeated micro-seeding. All crystals were cryoprotected with a reservoir solution supplemented with 15% glycerol.

Both native and SeMet-labelled *ct*SPD$^{1663–2223}$ crystals were grown by mixing equal volumes of the protein solution (11 mg ml^{-1}) with the precipitant solution containing 0.2 M ammonium citrate tribasic (pH 7.0), 20% PEG3350, and 10 mM DTT. Diffraction data were collected at beamline BL8.2.1 at the Advanced Light Source (Lawrence Berkeley National Laboratory) at the wavelength of 0.9786 Å at 100 K and processed with HKL3000 (ref. 32).

For crystallization of *ct*SPD$^{1632–2223}$–AMK and *ct*SPD$^{1693–2223}$–pAMK complexes, the purified *ct*SPD proteins were mixed with the *ct*Scc1-AMK or phospho-*ct*Scc1-AMK peptide inhibitors (KareBay Biochem) at a molar ratio of 1:2.5, and incubated overnight at room temperature to form covalent complexes as monitored by SDS–PAGE. The complexes were further purified with a Superdex 200 10/300 GL size-exclusion column in the buffer containing 20 mM Tris-HCl (pH 8.0), 200 mM NaCl, and 5 mM DTT. Crystals of *ct*SPD$^{1632–2223}$–AMK were grown by mixing equal volumes of the protein solution (13 mg ml^{-1}) with the precipitant solution containing 0.1 M ammonium citrate tribasic (pH 7.0) and 12% PEG3350. For the crystallization of *ct*SPD$^{1693–2223}$–pAMK complex, the 11 mg ml^{-1} protein solution was mixed with an equal volume of the precipitant solution containing 0.2 M KCl, 50 mM HEPES (pH 7.5), 32% pentaerythritol propoxylate (5/4 PO/OH), and 10 mM DTT. Diffraction data for *ct*SPD$^{1632–2223}$–AMK and *ct*SPD$^{1693–2223}$–pAMK were collected at beamline 19-ID (SBC-CAT) at the Advanced Photon Source (Argonne National Laboratory) at 100 K at wavelengths of 0.9793 Å and 0.9795 Å, respectively, and processed with HKL3000.

Structure determination and refinement. The crystal of SeMet-labelled *ct*SPD$^{1663–2223}$ diffracted to a minimum Bragg spacing of 2.20 Å and exhibited the symmetry of space group $P2_12_12_1$ with cell dimensions of $a = 55.67$ Å, $b = 98.79$ Å, $c = 107.76$ Å. Phases were obtained from the selenium single-wavelength anomalous diffraction method. With data truncated to 2.5 Å, nine of ten possible selenium sites were located and refined with PHENIX AutoSol[33], resulting in an overall figure of merit of 0.323. The experimental electron density map was used to construct an initial model with automated building with PHENIX AutoBuild. As a result, 414 of total 587 residues were built in the initial model, with R_{work} and R_{free} of 27.74% and 32.79%, respectively. Iterative model building and refinement were performed with JLigand[34], COOT[35], and PHENIX. Phases of native *ct*SPD$^{1663–2223}$, *ct*SPD$^{1632–2223}$–AMK, and *ct*SPD$^{1693–2223}$–pAMK were obtained by molecular replacement with Phaser using the SeMet crystal structure as the search model. Data collection and structure refinement statistics are summarized in Extended Data Table 1. Ramachandran statistics (favoured/allowed/outlier (%)) calculated by MolProbity[36] for *ct*SPD$^{1663–2223}$, *ct*SPD$^{1632–2223}$–AMK, and *ct*SPD$^{1693–2223}$–pAMK were 98.0/1.6/0.4, 98.1/1.9/0.0, and 98.1/1.7/0.2, respectively. All structural figures were generated with the program PyMOL (http://www.pymol.org/) using the same colour and labelling schemes.

31. Van Duyne, G. D., Standaert, R. F., Karplus, P. A., Schreiber, S. L. & Clardy, J. Atomic structures of the human immunophilin FKBP-12 complexes with FK506 and rapamycin. *J. Mol. Biol.* **229,** 105–124 (1993).
32. Minor, W., Cymborowski, M., Otwinowski, Z. & Chruszcz, M. HKL-3000: the integration of data reduction and structure solution—from diffraction images to an initial model in minutes. *Acta Crystallogr. D* **62,** 859–866 (2006).
33. Adams, P. D. *et al.* PHENIX: a comprehensive Python-based system for macromolecular structure solution. *Acta Crystallogr. D* **66,** 213–221 (2010).
34. Lebedev, A. A. *et al.* JLigand: a graphical tool for the CCP4 template-restraint library. *Acta Crystallogr. D* **68,** 431–440 (2012).
35. Emsley, P. & Cowtan, K. Coot: model-building tools for molecular graphics. *Acta Crystallogr. D* **60,** 2126–2132 (2004).
36. Chen, V. B. *et al.* MolProbity: all-atom structure validation for macromolecular crystallography. *Acta Crystallogr. D* **66,** 12–21 (2010).

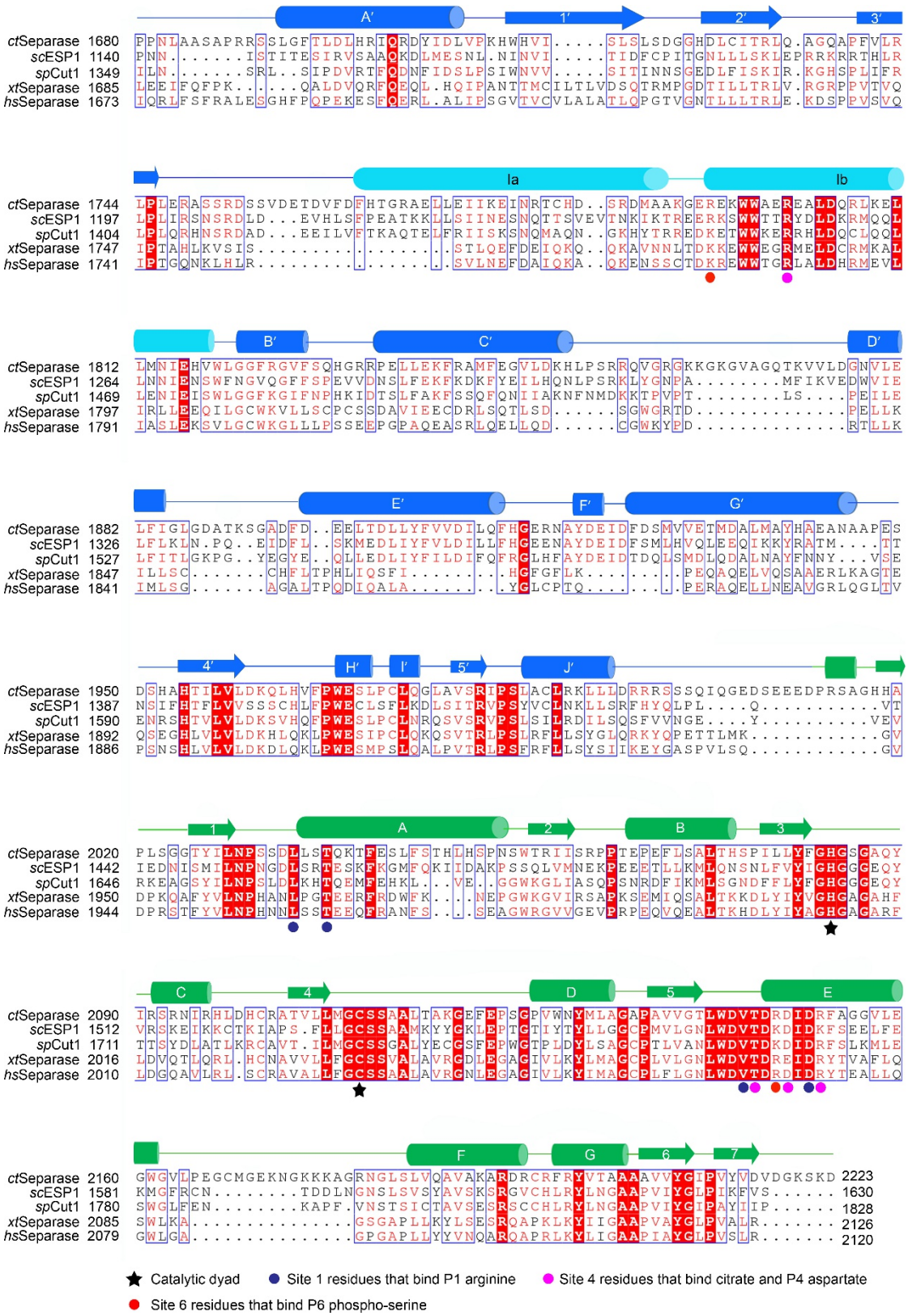

Extended Data Figure 1 | Sequence alignment of the SPDs from multiple species. The alignment is generated using the online ESPript 2.0 server. Secondary structural elements of *ct*SPD are indicated above the sequences, with the same labelling and colour schemes as in Fig. 1d (PPD, blue; APD, green; the helical insert in PPD, cyan). Abbreviations: *ct*, *Chaetomium thermophilum*; *sc*, *Saccharomyces cerevisiae*; *sp*, *Schizosaccharomyces pombe*; *xt*, *Xenopus tropicalis*; *hs*, *Homo sapiens*.

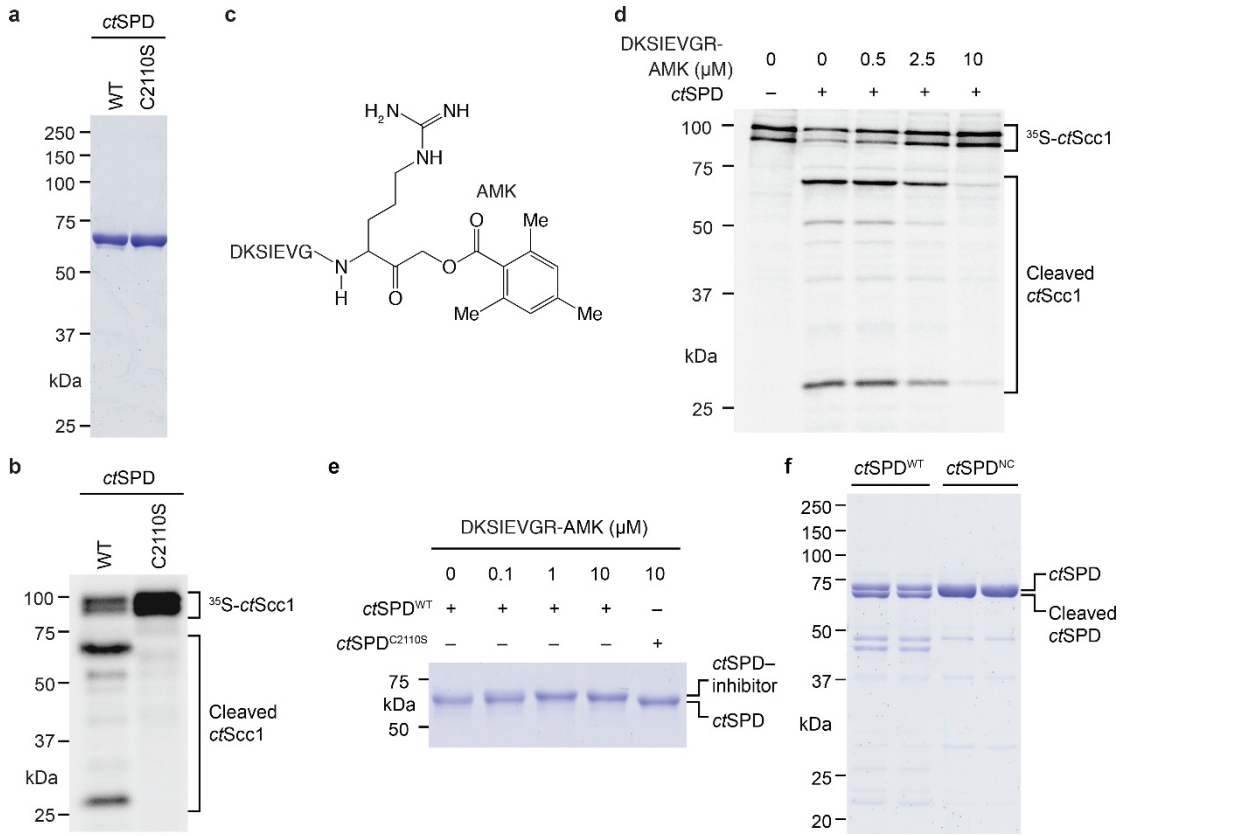

Extended Data Figure 2 | Purification, activity, inhibition, and autocleavage of active *ct*SPD. a, Coomassie-stained gel of purified recombinant *ct*SPD wild type (WT) and C2110S. **b**, Autoradiograph of the *ct*SPD cleavage assay with ^{35}S-*ct*Scc1 as substrate. **c**, Chemical structure of the acyloxymethyl ketone (AMK) inhibitor derived from the *ct*Scc1 cleavage site. **d**, Autoradiograph of the *ct*SPD cleavage assay with ^{35}S-*ct*Scc1 as substrate, in the absence or presence of increasing doses of the AMK inhibitor depicted in **c**. **e**, Coomassie-stained SDS–PAGE gel of purified recombinant *ct*SPD WT or C2110S treated with the indicated doses of the *ct*Scc1-AMK peptide inhibitor. The positions of unmodified *ct*SPD and *ct*SPD–inhibitor conjugates are indicated. **f**, Coomassie-stained gel of recombinant *ct*SPD$^{1632–2223}$ WT or non-cleavable (NC) mutant. The *ct*SPD^{NC} mutant contains the E1643R and R1646E mutations. The positions of intact and autocleaved *ct*SPD proteins are indicated.

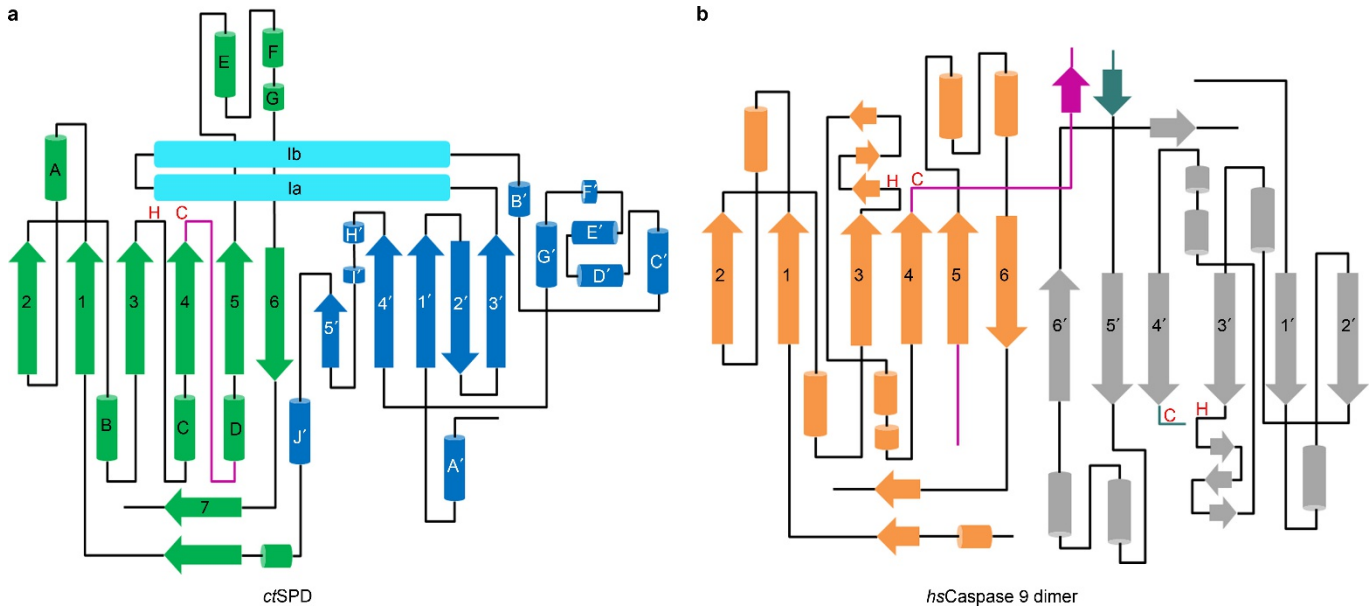

Extended Data Figure 3 | Comparison between the folding topologies of *ct*SPD and the caspase 9 dimer (Protein Data Bank accession number 1JXQ). The labelling and colour schemes are the same as in Fig. 1d, e. H, the catalytic histidine; C, the catalytic cysteine.

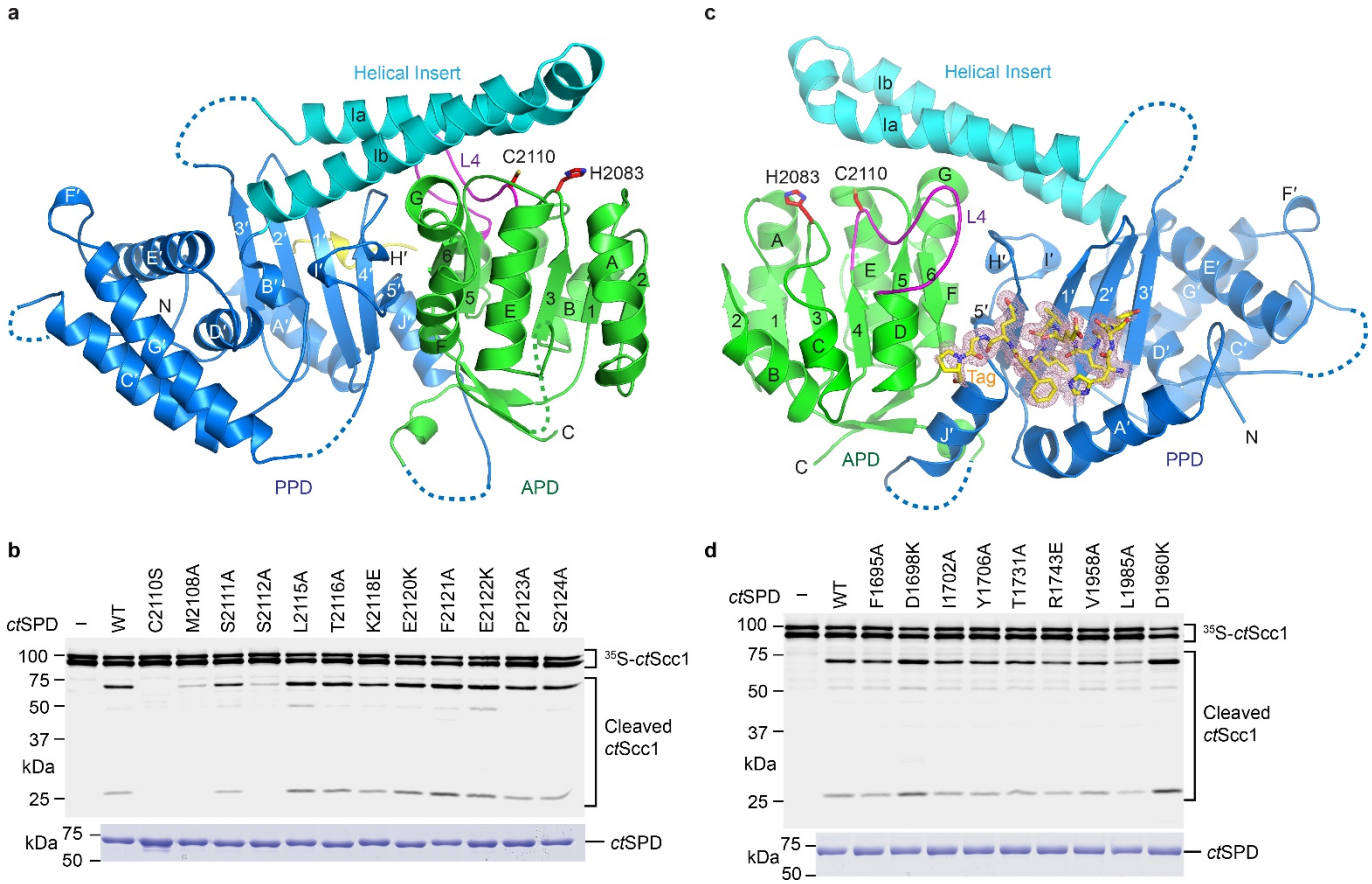

Extended Data Figure 4 | Contributions of the L4 loop and a surface pocket to the protease activity of *ct*SPD. a, Cartoon of the crystal structure of *ct*SPD, with the PPD coloured blue, the APD coloured green, the helical insert in PPD coloured cyan, and an N-terminal tag peptide coloured yellow. The N and C termini are indicated. All secondary structure elements are labelled. Loops with no visible electron densities are indicated by dashed lines. Loop 4 (L4) is coloured magenta. H2083 and C2110 of the catalytic dyad are shown as sticks. The orientation of *ct*SPD in this figure is related to that in Fig. 1d by a 180° rotation along the vertical axis. **c**, Representative autoradiograph of the ^{35}S-*ct*Scc1 cleavage assay by WT *ct*SPD or the indicated mutants. Bottom: Coomassie-stained gel of *ct*SPD proteins used in the assay. Quantification of the relative protease activities of *ct*SPD WT and mutants is shown in Fig. 2b. The protease activity is defined as the ratio between intensities of the two major *ct*Scc1 cleavage products and that of the uncleaved *ct*Scc1. **c**, Cartoon of the crystal structure of *ct*SPD, in the same orientation as in Fig. 1d. The tag peptide (HSQLEVLFQGP) is shown as sticks, overlaid with its $2F_o - F_c$ electron density map contoured at 1.0σ. **d**, Representative autoradiograph of the ^{35}S-*ct*Scc1 cleavage assay by WT *ct*SPD or the indicated mutants. Bottom: Coomassie-stained gel of *ct*SPD proteins used in the assay. Quantification of the relative protease activities of *ct*SPD WT and mutants is shown in Fig. 2d.

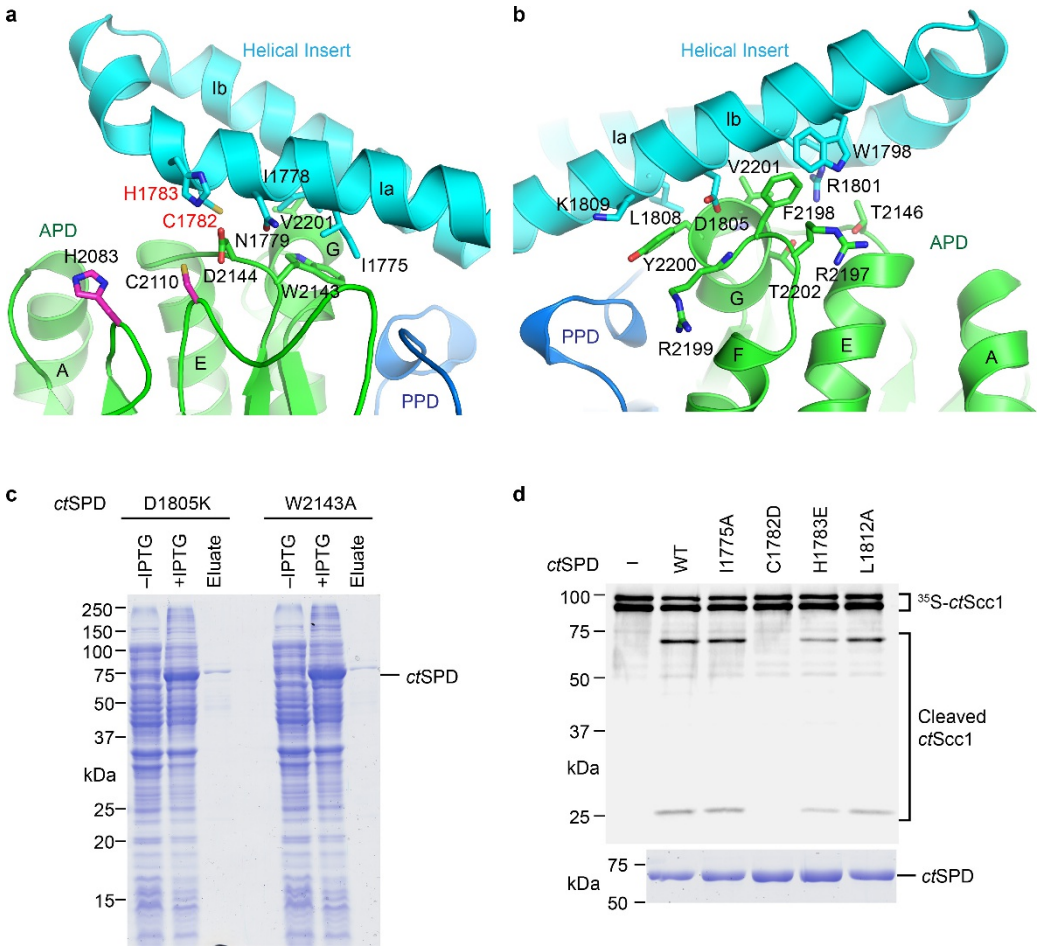

Extended Data Figure 5 | Interactions between the helical insert and the APD. a, **b**, Zoomed-in views of cartoons of *ct*SPD in two orientations that are related by a 180° rotation along the vertical axis. Residues at the interface between the helical insert of the PPD and the APD are shown in sticks and labelled. **c**, Coomassie-stained gel of lysates of bacteria expressing the indicated *ct*SPD mutants and treated without (–) or with (+) isopropyl β-D-1-thiogalactopyranoside (IPTG) and eluates from Ni^{2+}-NTA beads that had been incubated with the IPTG lysates. **d**, Autoradiograph of the ^{35}S-*ct*Scc1 cleavage assay by WT *ct*SPD or the indicated mutants. Bottom: Coomassie-stained gel of *ct*SPD proteins used in the assay.

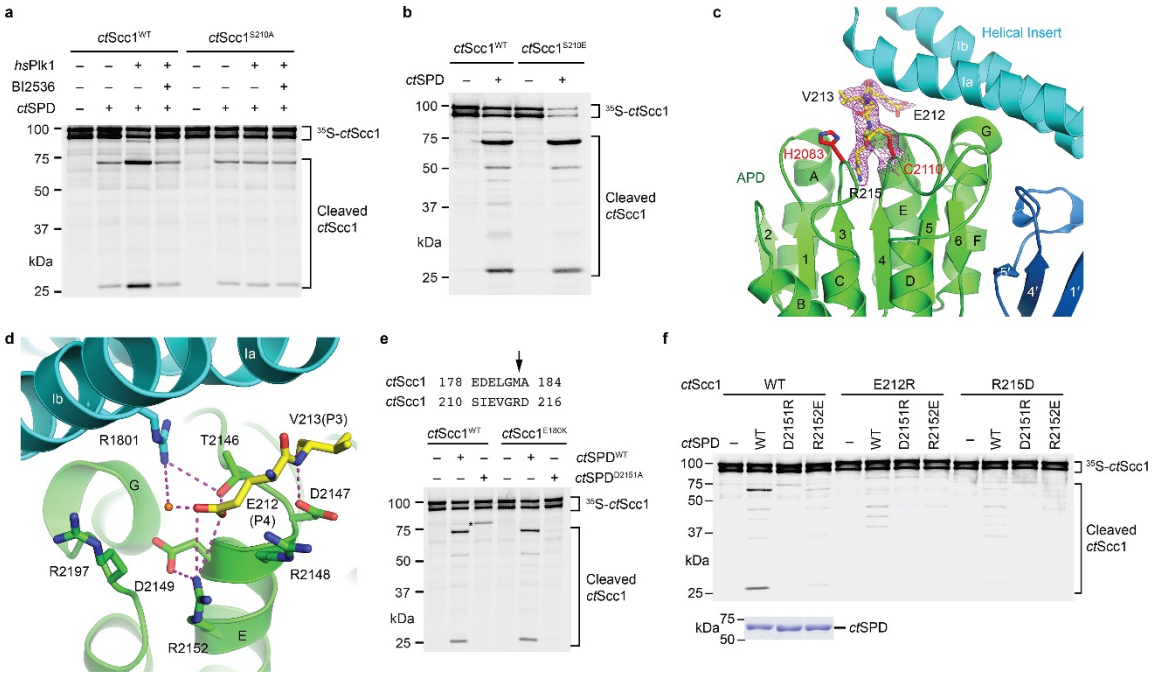

Extended Data Figure 6 | Phospho-regulation and specificity determinants of separase-mediated cohesin cleavage. a, Autoradiograph of the *ct*SPD cleavage reactions of ^{35}S-*ct*Scc1 WT or S210A, treated with or without human (*hs*) Plk1 or its inhibitor BI2536. **b**, Autoradiograph of the *ct*SPD cleavage reactions, with ^{35}S-*ct*Scc1 WT or the phospho-mimicking S210E as substrates. **c**, Zoomed-in view of the cartoon of *ct*SPD bound covalently to the *ct*Scc1-AMK inhibitor. The catalytic dyad residues C2110 and H2083 are shown as red sticks. The covalently bound inhibitor is shown as yellow sticks, overlaid with its $2F_o - F_c$ electron density map contoured at 1.0σ. **d**, Zoomed-in view of the S4 pocket of *ct*SPD that recognizes the P4 glutamate. Dashed lines indicate hydrogen bonds or favourable electrostatic interactions. The orange sphere indicates a water molecule. **e**, Mapping of the aberrant *ct*Scc1 cleavage site by *ct*SPD D2151A. Top: sequence alignment of the aberrant site of D2151A and the major site of WT. Bottom: autoradiograph of the cleavage reactions of *ct*SPD^{WT} or *ct*SPD^{D2151A} with the indicated ^{35}S-*ct*Scc1 proteins as substrates. Asterisk marks the aberrant cleavage product by *ct*SPD^{D2151A}. **f**, Charge reversal mutants of *ct*SPD fail to cleave complementary charge reversal mutants of *ct*Scc1. Autoradiograph of the cleavage assay of WT *ct*SPD or the indicated mutants, with ^{35}S-*ct*Scc1 WT or mutants as substrates. Bottom: Coomassie-stained gel of *ct*SPD proteins used in the assay.

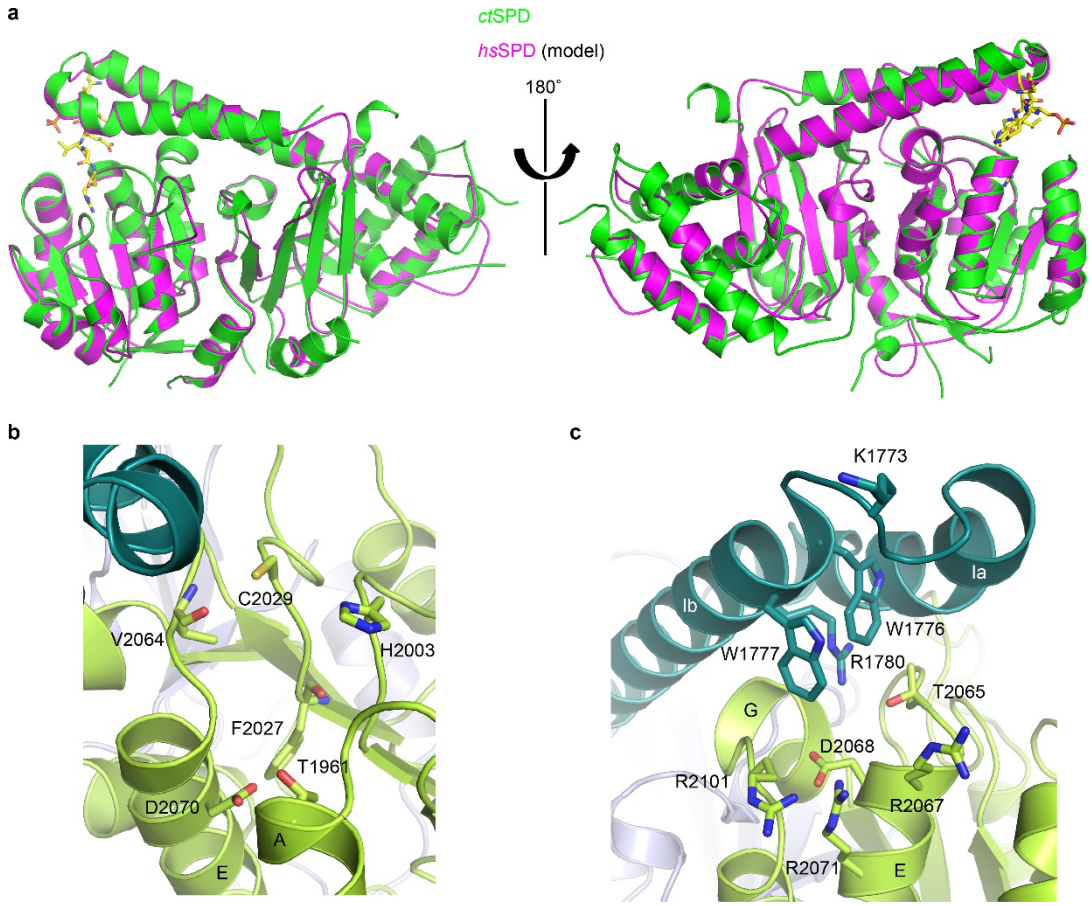

Extended Data Figure 7 | Conservation of substrate-binding residues in human separase. a, Two different views of the cartoon of the structure of *ct*SPD–pAMK (green) and a homology model of human (*hs*) SPD (magenta). The phospho-AMK peptide is shown in sticks. The homology model of *hs*SPD was generated with SWISS-MODEL. The coordinates of the model are available upon request. **b**, **c**, Zoomed-in views of the S1 and S4 pockets of the *hs*SPD model.

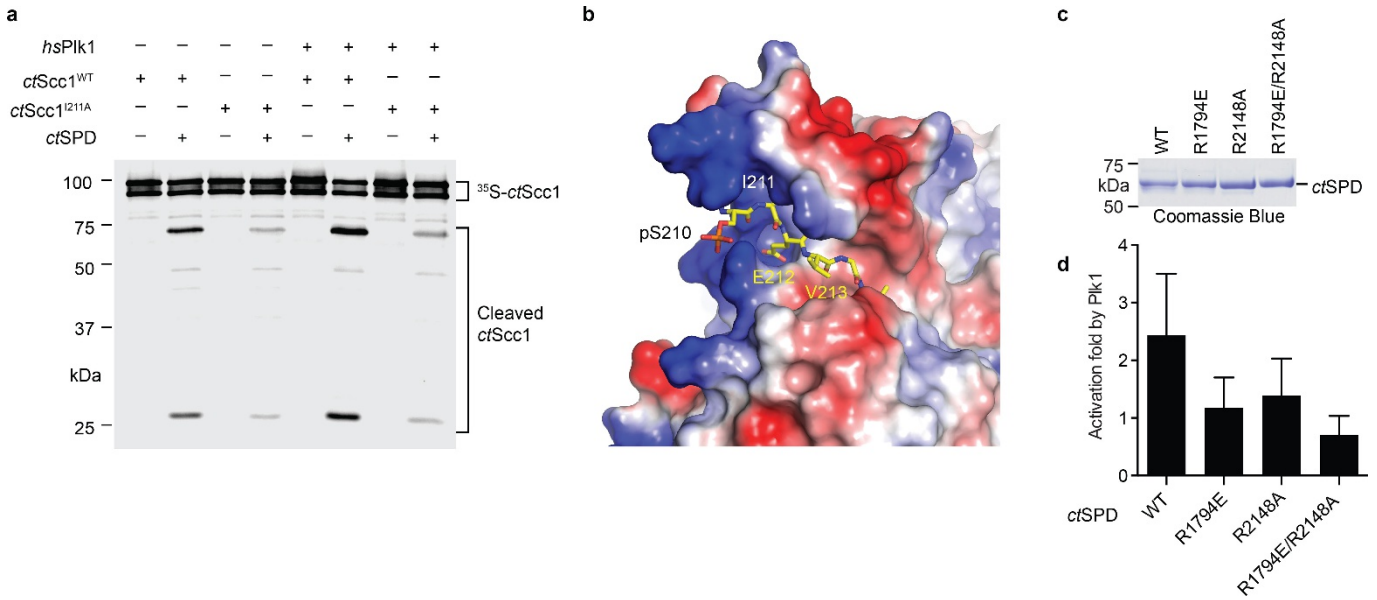

Extended Data Figure 8 | Structural basis of phosphorylation-stimulated Scc1 cleavage. a, Autoradiograph of the *ct*SPD cleavage reactions of ^{35}S-*ct*Scc1 WT or I211A, treated with or without *hs*Plk1. **b**, Zoomed-in view of the surface drawing of *ct*SPD–pAMK. The surface is coloured according to the electrostatic potential, with red, blue, and white representing negative, positive, and neutral charges, respectively. The covalently bound peptide is shown as sticks. **c**, Coomassie-stained gel of the indicated *ct*SPD proteins used in the assays described in Figs 3f and 4c. **d**, Quantification of the fold of Plk1 stimulation in *ct*Scc1 cleavage by *ct*SPD WT and the indicated mutants as described in Fig. 3f. Error bars, s.d. ($n = 3$ independent experiments).

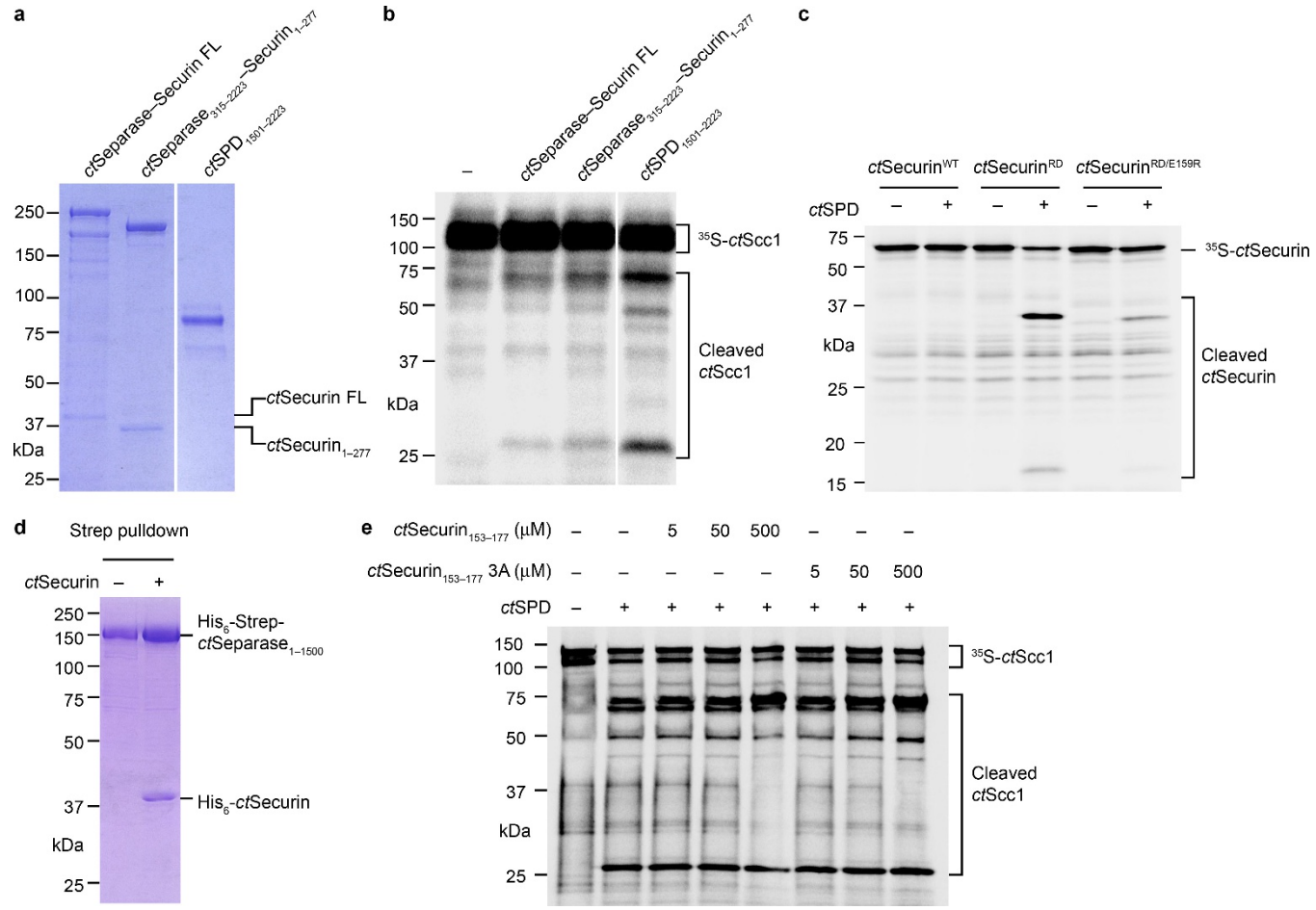

Extended Data Figure 9 | Interactions between *ct*securin and *ct*separase. **a**, Coomassie-stained gel of recombinant *ct*separase–*ct*securin complexes and *ct*SPD expressed in insect cells. FL, full length. **b**, Autoradiograph of the *ct*Scc1 cleavage reactions by the *ct*separase–*ct*securin complexes and *ct*SPD. **c**, Autoradiograph of the cleavage reactions of ^{35}S-*ct*securin WT or mutants with or without *ct*SPD. **d**, Coomassie-stained gel of recombinant Strep-tagged *ct*separase$_{1–1500}$ or the *ct*separase$_{1–1500}$–*ct*securin complex bound to Strep-Tactin beads. **e**, Autoradiograph of the *ct*Scc1 cleavage reactions by *ct*SPD, in the absence or presence of varying concentrations of the *ct*securin$_{153–177}$ or *ct*securin$_{153–177}$ 3A peptides. The EVE motif is mutated to AAA in the *ct*securin$_{153–177}$ 3A peptide.

Extended Data Table 1 | Data collection and refinement statistics

	*ct*SPD$^{1663\text{-}2223}$	*ct*SPD$^{1632–2223}$–AMK	*ct*SPD$^{1693–2223}$–pAMK
Data collection			
Space group	$P2_12_12_1$	$P6_322$	$P2_12_12_1$
Cell dimensions			
a, *b*, *c* (Å)	55.56, 98.89, 107.75	149.15, 149.15, 115.63	56.35, 85.01, 119.27
α, β, γ (°)	90, 90, 90	90, 90, 120	90, 90, 90
Resolution (Å)	50.00-1.90 (1.93-1.90) *	50.00-3.10 (3.15-3.10)	50.00-1.85 (1.88-1.85)
R_{merge} (%)	7.4 (97.0)	15.5 (100)	13.5 (100)
$I / \sigma I$	27.7 (2.5)	14.6 (1.3)	19.8 (1.9)
Completeness (%)	100 (100)	99.9 (98.7)	100 (100)
Redundancy	7.2 (7.3)	9.6 (8.7)	7.5 (5.8)
Refinement			
Resolution (Å)	49.38-1.90	48.82-3.10	42.51-1.85
No. reflections	46925	14228	50139
R_{work} / R_{free}	17.3 / 20.0	19.4 / 25.8	18.0 / 20.7
No. atoms			
Protein	3937	3745	3730
Ligand/ion	13	36	134
Water	394	52	454
B-factors			
Protein	27.4	78.4	26.6
Ligand/ion	32.6	86.0	29.8
Water	37.1	66.3	38.4
R.m.s deviations			
Bond lengths (Å)	0.012	0.010	0.013
Bond angles (°)	1.24	1.13	1.05

Data were collected from one crystal for each structure.
*Highest-resolution shell is shown in parenthesis.